Photoelectric effect with a twist

Giovanni De Ninno[1,2], Jonas Wätzel[3], Primož Rebernik Ribič[1,2], Enrico Allaria[1], Marcello Coreno[4,1], Miltcho B. Danailov[1], Christian David[5], Alexander Demidovich[1], Michele Di Fraia[1], Luca Giannessi[1,6], Klavs Hansen[7,8], Špela Krušič[9], Michele Manfredda[1], Michael Meyer[10], Andrej Mihelič[9], Najmeh Mirian[1], Oksana Plekan[1], Barbara Ressel[2], Benedikt Rösner[5], Alberto Simoncig[1], Simone Spampinati[1], Matija Stupar[2], Matjaž Žitnik[9], Marco Zangrando[1,11], Carlo Callegari[1], Jamal Berakdar[3]

[1]*Elettra-Sincrotrone Trieste S.C.p.A., 34149 Trieste, Italy*
[2]*University of Nova Gorica, 5000 Nova Gorica, Slovenia*
[3]*Institut für Physik, Martin-Luther Universität Halle-Wittenberg, 06099 Halle (Saale), Germany*
[4]*ISM-CNR, in Basovizza Area Science Park, 34149 Trieste, Italy*
[5]*Paul Scherrer Institut, 5232 Villigen-PSI, Switzerland*
[6]*INFN-LNF, Via E. Fermi 40, 00044 Frascati (Rome), Italy*
[7]*Center for Joint Quantum Studies and Department of Physics, Tianjin University, 92 Weijin Road, Tianjin 300072, China*
[8] *Dept. of Physics, Gothenburg University, 41296 Gothenburg, Sweden*
[9]*J. Stefan Institute, Jamova cesta 39, SI-1000 Ljubljana, Slovenia*
[10] *European XFEL GmbH Holzkoppel 4 22869 Schenefeld, Germany*
[11]*Istituto Officina dei Materiali, Consiglio Nazionale delle Ricerche, Basovizza, Italy.*

Photons have fixed spin and unbounded orbital angular momentum (OAM). While the former is manifested in the polarization of light, the latter corresponds to the spatial phase distribution of its wave front [1]. The distinctive way in which the photon spin dictates the electron motion upon light-matter interaction is the basis for numerous well-established spectroscopies that reveal the electronic, magnetic and structural properties of matter. In contrast, imprinting OAM on a matter wave, specifically on a propagating electron, is generally considered very challenging and the anticipated effect undetectable [2]. Indeed, this amounts to transferring the phase of a classical electromagnetic wave, defined within several hundreds of nanometres, to a quantum particle localized within the few angstroms of an atom. In addition, the centre of symmetry of irradiated atoms does not in general coincide with the axis of the photon beam. In [3], the authors provided evidence of OAM-dependent absorption of light by a cold trapped atom, located in the centre of the light beam. Off-centre excitation was studied in [4]. Here we seek to observe an OAM-dependent dichroic photoelectric effect, using an extended sample of He atoms. Surprisingly, we find experimentally, and confirm theoretically, that the OAM of an optical field can be imprinted coherently onto a propagating electron wave, and that this phase information survives ensemble averaging out to macroscopic distances, where the electron is detected. We also show that electronic transitions, which are otherwise optically inaccessible due to selection rules, are essential for this process to occur. Our results reveal new aspects of light-matter interaction and point to a new kind of single-photon electron spectroscopy for accessing electronic optical transitions that are usually forbidden by symmetry.

In our experiment, He atoms are ionized by XUV radiation, generated by a free-electron laser (FEL) [5], in the presence of an intense infrared (IR) laser field, see Fig.

1a. The FEL beam is in a fixed (right-handed) circular polarization state, $\sigma_{\text{FEL}} = +1$. What happens if the IR field has a vortex phase profile carrying OAM? Is it possible to observe a vortex-dependent dichroic effect that depends on the sign of the OAM, even though the atoms are randomly distributed across the profile of the OAM beam? This would be surprising: the atomic wave function is extremely localized on the scale of the OAM beam's waist, see Fig. 1b. Off-axis atoms experience the IR laser field as an ordinary Gaussian beam [6] and atoms close to the optical axis, where the OAM is well defined, experience a vanishingly small field [7]; besides, the fraction of near-axis atoms is small. While the transfer of optical OAM to photoelectrons seems unlikely, if it happens, it should involve a new type of non-dipole transitions [7,6], related to the OAM-carrying vector potential, which could be used, e.g., to optically induce orbital magnetization in molecules [8].

To investigate the possibility of observing a vortex-dependent dichroic effect on randomly distributed electrons, we used an IR laser with adjustable right or left-handed circular polarization ($\sigma_{\text{IR}} = \pm 1$), and variable amount $m_{\text{OAM}} \hbar$ of OAM, where m_{OAM} is a signed integer, called topological charge. The two light beams are focused and overlapped with a gas jet of He atoms in a vacuum chamber equipped with a velocity map imaging (VMI) spectrometer [9]. The velocity distribution of electrons produced in the interaction volume is projected onto a 2D imaging detector. For high enough IR intensities, the resulting photoelectron spectra, see Figs. 1c and 1d, show a main band, corresponding to direct (XUV-induced) photoemission, together with a series of weaker rings, called sidebands, whose radius increment (decrement) represents the energy acquired (lost) by the photo-emitted electrons upon absorption (emission) of one or more IR photons. All bands depend on the polar angle at which photoelectrons are emitted [10, 11]. They reflect the interplay between XUV and optical fields during the photoionization process [12,13], providing information on the transfer of light properties, e.g., angular momentum, to matter [14-17]. When the two beams are circularly polarized and $m_{\text{OAM}} = 0$, there is a few-percent difference in the angular electron distributions for co-rotating and counter-rotating XUV and IR fields, resulting in a dichroism contrast in the range 5-10% [18-21].

Now what happens if $m_{\text{OAM}} = \pm 1$. The two VMI spectra shown in Figs. 1c and 1d have been obtained for fixed IR polarization ($\sigma_{\text{IR}} = +1$) and alternate OAM ($+\hbar$ and $-\hbar$, respectively), with all other experimental conditions kept unchanged. The images demonstrate that different topological charges result in qualitatively different photoelectron spectra, attesting a clear OAM-dependent dichroic effect. This is a first proof of the possibility to imprint *virtually unbounded* photon OAM on the matter wave of a propagating electron.

To clarify the underlying physics of OAM-dependent dichroism we developed a first-principle theoretical model that accounts for all non-linear effects in light-matter interaction (see Supplementary Material) and amounts to a numerical solution of the three-dimensional, time-dependent Schrödinger equation for the lasers-driven atom, and an averaging over the atoms ensemble in the lasers spots. Analytically, insight into the important contributions is possible by considering a single atom centred on the optical axis and a weak IR field. Ionization upon absorption of one XUV photon with frequency ω_{FEL} followed by the absorption of one IR photon with frequency ω_{IR} is described by the two-photon ionization amplitude:

$$M(f, \omega_{FEL}, \omega_{IR}) = \frac{1}{i} \lim_{\varepsilon \to 0^+} \sum_v \frac{\langle f | H_{\text{int}}^{\text{IR}} | v \rangle \langle v | H_{\text{int}}^{\text{FEL}} | 1s \rangle}{E_{1s} + \omega_{\text{FEL}} - E_v + i\varepsilon}.$$

100 The electron is excited from the ground state $|1s\rangle$, having energy E_{1s}, to the final state
101 $|f\rangle$, passing through intermediate states $|v\rangle$, having energies E_v. Both lasers propagate
102 in the same direction, which is taken as the quantization axis. The dipole transition
103 due to the FEL-atom interaction, mediated by $H_{\mathrm{int}}^{\mathrm{FEL}}$, determines the angular
104 distribution of the (continuum) intermediate states $|v\rangle$, described by the spherical
105 harmonics $Y_{l=1,m=\sigma_{\mathrm{FEL}}}(\vartheta_k, \varphi_k)$, where (ϑ_k, φ_k) are the polar and azimuthal spherical
106 angles specifying the electron linear-momentum (k) direction. The quantum numbers
107 $l = 1$, $m = \sigma_{\mathrm{FEL}}$ reflect the symmetry of the electric dipole operator. The
108 corresponding photoelectron distributions are shown in the middle part of Figs. 2a and
109 2b. The OAM is transferred to the electron via a continuum-continuum transition
110 through the action of the IR-atom interaction matrix element, $\langle f|H_{\mathrm{int}}^{\mathrm{IR}}|v\rangle$. Hence, the
111 energy and angular distribution of the final state is encoded into the first outer (IR
112 absorption) or inner (IR emission) sideband. It can be shown (see Methods) that at
113 short distance, ρ, from the optical axis, $H_{\mathrm{int}}^{\mathrm{IR}}$ can be decomposed into a contribution
114 stemming from the *longitudinal* electric field component [22], scaling as $(\rho/$
115 $w_0)^{|m_{\mathrm{OAM}}+\sigma_{\mathrm{IR}}|}$, where w_0 is the waist of the IR beam, and another due to the
116 *transverse* field component, scaling as $(\rho/w_0)^{|m_{\mathrm{OAM}}|}$. The interplay between photon
117 OAM and spin plays a crucial role: in the *parallel case*, i.e., for $m_{\mathrm{OAM}} = \sigma_{\mathrm{IR}} = +1$,
118 the longitudinal component scales as $(\rho/w_0)^2$, and the transverse component like
119 (ρ/w_0). Near the optical axis, where $(\rho/w_0) \ll 1$, the continuum-continuum matrix
120 element $\langle f|H_{\mathrm{int}}^{\mathrm{IR}}|v\rangle$ contributes with a dominant quadrupole transition, governed by
121 the selection rule $\Delta l = 2, \Delta m = 2$, leading to an asymptotic momentum distribution
122 proportional to $Y_{3,3}(\vartheta_k, \varphi_k)$. As shown in the top part of Fig. 2a, such a function has a
123 donut-like shape, extending in the transverse plane. In contrast, in the *antiparallel*
124 *case*, i.e., for $\sigma_{\mathrm{IR}} = -m_{\mathrm{OAM}} = +1$, a strong on-axis longitudinal component scaling
125 as $(\rho/w_0)^0 = 1$ is manifested, while the transverse component scales again as
126 (ρ/w_0). Consequently, the latter can be neglected and the continuum-continuum
127 transition is dominated by a dipolar term, with the selection rule $\Delta l = 1, \Delta m = 0$,
128 which forms the electron density in the longitudinal direction, see top part of Fig 2b.
129 The different combinations of σ_{IR} and m_{OAM} we have considered in this work,
130 together with the selection rules for the corresponding transitions, are shown in the
131 inset of Fig. 2b.
132 The projection of the solution of the Schrödinger equation on above-threshold
133 continuum states yields the differential cross sections (DCSs) for a given electron
134 kinetic energy. Therefore, the calculated DCSs can be directly compared to the
135 sideband area, as a function of the polar angle, obtained experimentally using the
136 VMI spectrometer. However, in order to make this comparison possible, one needs to
137 move from the single-atom picture to the real-world ensemble average. For that
138 purpose, the problem is solved for atoms randomly distributed in the whole FEL and
139 IR spots and the results are then averaged. As shown in Figs. 3a and 3b, the average
140 does not substantially change the shape of the electron distribution when the spin and
141 OAM are *parallel*, while it has a quite evident effect when the momenta are
142 *antiparallel*. In the latter case, as shown in Fig. 3c, the calculated average DCS for the
143 first outer sideband shows a peak in the transverse direction (i.e., $\vartheta_k = \pi/2$), whereas
144 the single-electron DCS (Fig. 2b, top part) shows a minimum. However, as shown in
145 Fig. 3d, a clear dichroic effect is still visible. The insets of Figs. 3a and 3b show the
146 projection of the photoelectron distributions on the (k_y, k_z)plane. Such projections can

147 be directly compared to the experimental VMI images.

148 For a more direct comparison with theoretical results, we collected data at low IR
149 intensity, enabling a straightforward interpretation of the VMI images by means of
150 first-order processes. The VMI image obtained for the case $\sigma_{IR} = +1, m_{OAM} = -1$ is
151 shown in Fig. 4a, while Fig. 4b shows the corresponding theoretical prediction. The
152 qualitative agreement is very good. By acquiring data for different combinations of
153 the IR spin and OAM, we extracted the DCS for the first sideband, after Abel
154 inversion of the VMI spectra [23]. As a benchmark, we first considered the case
155 $\sigma_{IR} = \pm 1$, with $m_{OAM} = 0$ (i.e., standard, spin-dependent, dichroism). We obtained a
156 good agreement between experiments and theory, and results similar to the ones
157 reported in [21] (data not shown). Then, we focused on the cases wit   h   nonzero
158 OAM. Fig. 4c shows the DCSs for the cases $\sigma_{IR} = +1, m_{OAM} = +1$ and $\sigma_{IR} = $
159 $+1, m_{OAM} = -1$, together with the OAM-dependent dichroism as a function of the
160 polar angle. Fig. 4d reports the corresponding theoretical predictions. The agreement
161 between experiment and theory is good: in both cases there is a clear OAM-dependent
162 dichroic effect, which is maximum, i.e., about $(7.5 \pm 1.2)\%$, at about $\vartheta_k = \pi/2$ (for a
163 discussion on the evaluation of both statistical and systematic errors, see Methods). A
164 similar good agreement was found for switched OAM and switched polarizations, see
165 Figs. 4e and 4f, and for fixed OAM and switched polarizations, see Figs. 4g and 4h.
166 Note that in the former case nonzero dichroism is present at all angles, in the range 3-
167 7%, depending on the value of ϑ_k, while in the latter significant dichroism, about
168 $(2.5 \pm 1.3)\%$, is observed at $\vartheta_k = \pi/4$ and $\vartheta_k = 3\pi/4$.
169 Summarizing, we confirm that the spatial distribution of an optical field with vortex
170 phase profile can be imprinted coherently on a photoelectron wave packet that recedes
171 from atoms randomly distributed over the laser spot. The large dimension acquired by
172 the electron wave function during the two-colour continuum-continuum process is the
173 key for explaining the success of our experiment, in spite of the very different size of
174 atoms and OAM beam's waist. Indeed, the OAM-carrying IR beam acts on the
175 electron wave function after the latter is inflated, following the XUV-induced atom
176 ionization. The propagating photoelectron wave can scan over the spatial topology of
177 the IR field, acquiring OAM. Instead, a direct ionization with XUV OAM photons
178 produces essentially OAM-independent photoelectrons [2]. The observed effect is
179 traced back to non-dipole transitions and to the transverse component of the light
180 wave. Larger dichroic contrasts may be expected by using a probe beam carrying
181 higher OAM, or by considering higher-order sidebands, corresponding to multi-
182 photon absorption. Our results explore new aspects of light-matter interaction and
183 point to qualitatively novel analytical tools, which can be used (e.g.) to study the
184 instric chiral structure of compex organic molecules.
185
186 **Methods**
187
188 *Experiment*. The experiment was carried out at the LDM beam line of the FERMI
189 FEL [5]. Right-hand circularly polarized XUV pulses at 28.5 eV (43.5 nm), with a
190 bandwidth of about 94 meV (0.05 nm) and a duration of about 100 fs were delivered
191 by APPLE II-type undulators, via the Photon Analysis Delivery and REduction
192 System (PADRES) [24]. The average pulse energy was 80±10 μJ, with a repetition
193 rate of 10 Hz. Active mirrors in Kirkpatrick–Baez configuration [25] focused the FEL
194 pulses to a spot size of about 10 μm diameter (full width at half maximum). Taking
195 into account the theoretical overall transmission of all optical components in the
196 beamline (about 60%), average intensities up to 10^{18} W/m^2 were reached in the
197 interaction region [26]. Near IR pulses from a Ti:Sa laser (1.58 eV; 784 nm) were

used, with variable (right and left-handed, $\sigma_{IR} = \pm 1$) circular polarization, generated using a combination of a half wave plate and a quarter wave plate, and variable topological charge ($m_{OAM} = \pm 1$), generated using a phase mask. The IR pulse bandwidth was 13 nm (full width at half maximum) and its duration 175 fs. The pulse energy was varied in the range 120-800 μJ. With a spot size of 60±10 μm, and taking into account optics efficiency and transmission, the intensity range at the sample position was 0.5 - 4 × 10^{17} W/m^2. The highest IR pulse energy was used for the initial optimization and to obtain a first evidence of OAM-dependent dichroism (see Figs. 1c and 1d). Subsequently, a lower intensity (about 0.7 × 10^{17} W/m^2) was employed for collecting the results to be compared with theoretical predictions. The IR pulses were produced by splitting the FEL-seeding pulses, providing a very stable two-colour synchronization. The FEL and the IR pulses were overlapped in time and space in the centre of the experimental chamber. The spatial overlap was determined by visual inspection of the images of both beams on a retractable Ce:YAG fluorescent screen. The system is based on a commercial digital camera and two achromatic doublets in a finite/finite-conjugate symmetric arrangement. The resolution of the optical system is 7 um, and a conservative estimate of the accuracy of visual overlap is 20 μm. The spatial overlap was also checked periodically by seeking the local minimum of the sideband signal while steering the IR beam. As for the case of visual overlap, a conservative estimate of the accuracy of this procedure is 20 um. The temporal overlap was controlled by a delay stage in the IR-laser delivery system and was optimized using first a coaxial cable antenna and then directly the two-colour two-photon signal. The VMI spectrometer includes a 75-mm diameter imaging quality multichannel plate (MCP) stack + phosphor screen, with a sCMOS camera for the image readout. Its electron optics were set to work optimally for the selected kinetic energies of He 1s electrons. A pulsed, supersonic He beam produced with a commercial Even–Lavie valve (aperture 260 μm) was used to provide sufficient gas density (about 10^{16} atoms per m^3) in the interaction region, allowing a shot-to-shot analysis of the VMI spectra.

Data analysis. The sCMOS camera (2,560×2,160 pixels; 6.5 μm pixel size) readout acquired single-shot pictures of the two-dimensional projection of the electron angular distribution [9]; only the central portion (900×900 pixels, corresponding to the maximum data flow that the camera can handle at the full repetition rate of the FEL) was acquired, corresponding to the full size of the phosphor screen. For low IR energy, i.e., for strong suppression of the signal of sidebands higher than one (see for example, Fig. 4a), these images were transformed into three dimensional momentum distributions with full angular reconstruction of the electron emission, by applying an Abel transformation [23]. The transformed images were then analysed by means of a MATLAB script, allowing to calculate the photoelectron yield of the first sideband, as a function of the polar angle. The analysis focused on the first outer sideband; the inner sideband, though carrying the same information, is affected by the overlap with the signal from the main band in the two-dimensional VMI image, leading to a higher statistical error. Dichroism was calculated as the difference between the DCSs corresponding to two specific sets of photon spin and OAM, normalized to the sum of the maxima of the same DCSs. The statistical error on the dichroic contrast (see Fig. 4) was estimated by calculating the number of electrons at some representative polar angles (i.e., $\vartheta_k = \pi/2$, $\pi/4$, $3/2\,\pi$) of the ring corresponding to the first sideband of the VMI images and assuming a Poisson-like error distribution. The number of electrons

247 located at $\vartheta_k = \pi/2$ is typically of the order of 3.5×10^3, giving an error of about 1.7%;

248 the number of electrons located at $\vartheta_k = \pi/4$ and $\vartheta_k = 3/2\pi$ is of the order of 10^3, giving

249 an error of about 3.2%. The uncertainty on the dichroic contrast, at a given ϑ_k, was

250 calculated by error propagation. The profile of the dichroic contrast is also affected by

251 a systematic error due to the lack of perfect reproducibility in the procedure for the

252 transverse alignment between the XUV and IR beams, which was carried out each

253 time, after flipping the OAM phase mask. As it was already mentioned, this procedure

254 has an estimated accuracy of 20 μm. Such an error is likely to be at the origin of the

255 small distortion in the profile of the dichroic contrasts shown in Fig. 4.

256

257 ***Theoretical model***. Within the single-active-electron approach, the time-dependent

258 three-dimensional Schrödinger equation was solved numerically on a fine space-time

259 grid ($\Delta r = 0.05$ a.u. and $\Delta t = 0.025$ a.u.), using an effective potential [27] and in the

260 presence of both laser fields. Our method relies on the representation of the wave

261 function in a spherical basis, i.e., using spherical coordinates $\boldsymbol{r} = \{r, \vartheta, \varphi\}$ relative to

262 atom's core: $\Psi(\boldsymbol{r}, t, \boldsymbol{b}) = \sum_{l,m} R_{l,m,\boldsymbol{b}}(r,t) Y_{l,m}(\vartheta, \varphi)$. Here, l and m are the orbital and

263 magnetic quantum numbers, respectively, while $R_{l,m}(r)$ is the radial wave function

264 for the angular channel l,m and $Y_{l,m}(\vartheta, \varphi)$ are spherical harmonics. The parameter $\boldsymbol{b}$

265 indicates the position of the considered atom relative to the (common) optical axes of

266 both laser fields. The initial condition is given by $\Psi(r, t \to -\infty, \boldsymbol{b}) =$

267 $\mathcal{R}_{1s,\boldsymbol{b}}(r) Y_{0,0}(\vartheta, \varphi)$, where $\mathcal{R}_{1s,\boldsymbol{b}}(r)$ is the radial wave function of the 1s electron in the

268 He ground state, at the shifted position $\boldsymbol{b}$. The wave-function is propagated to a time

269 $t = T_{\text{obs}}$, at which both laser fields are extinguished. Then, $\Psi(\boldsymbol{r}, t, \boldsymbol{b})$ is projected

270 onto a set of continuum states $\left|\phi_{\boldsymbol{k}}^{(-)}\right\rangle$, characterized by the asymptotic momentum $\boldsymbol{k}$

271 (with direction $\{\vartheta_{\boldsymbol{k}}, \varphi_{\boldsymbol{k}}\}$), to obtain the DCS, i.e. $\frac{d\sigma_{\boldsymbol{b}}}{d\Omega_{\boldsymbol{k}}} =$

272 $\left|\left\langle\phi_{\boldsymbol{k}}^{(-)}\middle|\Psi(T_{\text{obs}}, \boldsymbol{b})\right\rangle\right|^2$, where $d\Omega_{\boldsymbol{k}} = \sin\vartheta_{\boldsymbol{k}} \, d\vartheta_{\boldsymbol{k}} d\varphi_{\boldsymbol{k}}$.

273 Crucial is a proper description of the complete light-matter interaction Hamiltonian

274 operator which consists of two contributions: (i) $\widehat{H}_{\text{int}}^{\text{FEL}}(t) = \boldsymbol{A}_{\text{FEL}}(\boldsymbol{r} - \boldsymbol{b}, t) \cdot \boldsymbol{p} +$

275 $\frac{1}{2}\boldsymbol{A}_{\text{FEL}}(\boldsymbol{r} - \boldsymbol{b}, t)^2$ describing the action of the Hermite-Gaussian FEL pulse and (ii)

276 $\widehat{H}_{\text{int}}^{\text{IR}}(t) = \frac{1}{2}[\boldsymbol{p} \cdot \boldsymbol{A}_{\text{IR}}(\boldsymbol{r} - \boldsymbol{b}, t) + \boldsymbol{A}_{\text{IR}}(\boldsymbol{r} - \boldsymbol{b}, t) \cdot \boldsymbol{p} + \boldsymbol{A}_{\text{IR}}(\boldsymbol{r} - \boldsymbol{b}, t)^2] - \Phi_{\text{IR}}(\boldsymbol{r} - \boldsymbol{b}, t)$

277 for the vortex IR field. Here, we introduced the momentum operator $\boldsymbol{p}$,

278 while $\boldsymbol{A}_{\text{FEL}}(\boldsymbol{r}, t)$, $\boldsymbol{A}_{\text{IR}}(\boldsymbol{r}, t)$ and $\Phi_{\text{IR}}(\boldsymbol{r}, t)$ are the electromagnetic vector and scalar

279 potentials of the FEL and IR fields. The final DCS, which is compared to the

280 experimental VMI images, is obtained after averaging over N_A randomly distributed

281 atoms within the FEL spot, i.e., $\text{DCS}_{\text{total}} = \frac{1}{N_A}\sum_{\boldsymbol{b}} \frac{d\sigma_{\boldsymbol{b}}}{d\Omega_{\boldsymbol{k}}}$.

282 The vector potential of the IR vortex field with photon energy $\hbar\omega_{\text{IR}}$ (wave number

283 $k_{\text{IR}} = \omega_{\text{IR}}/c$) is given by $\boldsymbol{A}_{\text{IR}}(\boldsymbol{r}, t) = A_0^{\text{IR}} \boldsymbol{\epsilon}_{\text{IR}} u(\boldsymbol{r}) f(t) e^{i(k_{\text{IR}}z - \omega_{\text{IR}}t)} + \text{c.c.}$, where A_0^{IR}

284 is the amplitude and the transversal distribution function reads

285 $$u(\boldsymbol{r}) = \left(\frac{\sqrt{2}\rho}{\widetilde{w}(z)}\right)^{m_{\text{OAM}}} e^{-\frac{\rho^2}{\widetilde{w}^2(z)}} e^{i\left[m_{\text{OAM}}\varphi + \frac{k_{\text{IR}}\rho^2 z}{2(z^2+z_R^2)} - (m_{\text{OAM}}+1)\tan^{-1}z/z_R\right]},$$

286 with $\rho = r\sin\vartheta$ and $z = r\cos\vartheta$. Further, we introduce the beam waist w_{IR} which

287 determines both the beam width $\widetilde{w}(z) = w_{\text{IR}}\sqrt{1 + z^2/\tilde{z}_R^2}$, as well as the Rayleigh

288 range $\tilde{z}_R = k_{\text{IR}} w_{\text{IR}}^2/2$. The vector field is not solenoidal. Depending on the circular

289 polarization state (governed by $\boldsymbol{\epsilon}_{\text{IR}} = -\sigma_{\text{IR}}[\boldsymbol{\epsilon}_x + i\sigma_{\text{IR}}\boldsymbol{\epsilon}_y]/\sqrt{2}$, where $\boldsymbol{\epsilon}_x$ and $\boldsymbol{\epsilon}_y$ are the

290   Cartesian unit vectors) relative to the carried OAM, the emitted photoelectron may be
291   exposed to a strong scalar potential $\Phi_{IR}(\boldsymbol{r},t)$ (action of a longitudinal field). The
292   leading term scales as $\Phi_{IR}(\boldsymbol{r},t) \sim \frac{c}{k_{IR}}\left(\frac{\rho}{w_{IR}}\right)^{m_{OAM}+\sigma_{IR}} e^{ik_{IR}z}$ while the (transverse)
293   vector potential scales as $A_{IR}(\boldsymbol{r},t) \sim \left(\frac{\rho}{w_{IR}}\right)^{m_{OAM}}$ in the vicinity of the optical axis. As
294   a consequence, in the *parallel* case, i.e., for $m_{OAM} = \sigma_{IR}$, the transverse contribution
295   of the interaction Hamiltonian $\hat{H}_{int}^{IR}(t)$ dominates the continuum-continuum transition
296   to the side band energy. Indeed, under the present experimental conditions, $(\rho/$
297    $w_{IR}) \ll 1$ (w_{IR} being in the μm regime). Conversely, in the *antiparallel* case, i.e., for
298    $m_{OAM} = -\sigma_{IR}$, the electric scalar potential dominates and leads to a dipole transition.
299   Writing the interaction Hamiltonian in terms of spherical harmonics, the nature of the
300   electronic transitions to the first side band, in the presence of the IR laser and for $\boldsymbol{b} =$
301   0, becomes evident. The dominating first-order transitions, see inset of Fig. 2b, are
302   governed by the following selection rules, depending on the OAM and spin states of
303   the IR photon:

304   (i) $m_{OAM} = \sigma_{IR} = +1$: $|l = 1, m = 1\rangle \overset{IR}{\to} |l = 3, m = 3\rangle$, quadrupole transition
305   induced by the transverse component of the interaction Hamiltonian; rule:
306           $\Delta l = 2, \Delta m = 2$;

307   (ii) $m_{OAM} = -\sigma_{IR} = +1$: $|l = 1, m = 1\rangle \overset{IR}{\to} |l = 2, m = 1\rangle$, dipole transition
308   induced by the electric scalar potential (longitudinal field); rule: $\Delta l = 1$,
309           $\Delta m = 0$;

310   (iii) $m_{OAM} = \sigma_{IR} = -1$: $|l = 1, m = 1\rangle \overset{IR}{\to} \alpha|l = 1, m = -1\rangle + \beta|l = 3, m = -1\rangle$
311   (where α and β are complex coefficients), quadrupole transition induced by
312   the transverse component of the interaction Hamiltonian; rule: $\Delta l = 0,2$,
313           $\Delta m = -2$.

314

315

322

323   **Author contributions** GDN, PRR, JW and JB proposed the experiment, whose
324   feasibility was discussed with MC, MŽ and CC. GDN coordinated the experiment.
325   JW and JB developed the theoretical model and JW carried out the simulations. CC,
326   AM, BR, JW, KH, MC, MDF, MS, OP, ŠK, PRR and GDN carried out the
327   measurements. PRR, EA, AD, AS, BR, CD, MBD, MDF, MMa, MZ, NM and SS
328   prepared the light source. GDN, BR and MDF carried out the data analysis. GDN, JW
329   and JB wrote the first draft of the manuscript; the latter was first reviewed by AM,
330   BR, CC, MMe, MŽ and PRR and then discussed with all co-authors.

331

332

333

334

335

336
337
338
339
340
341
342
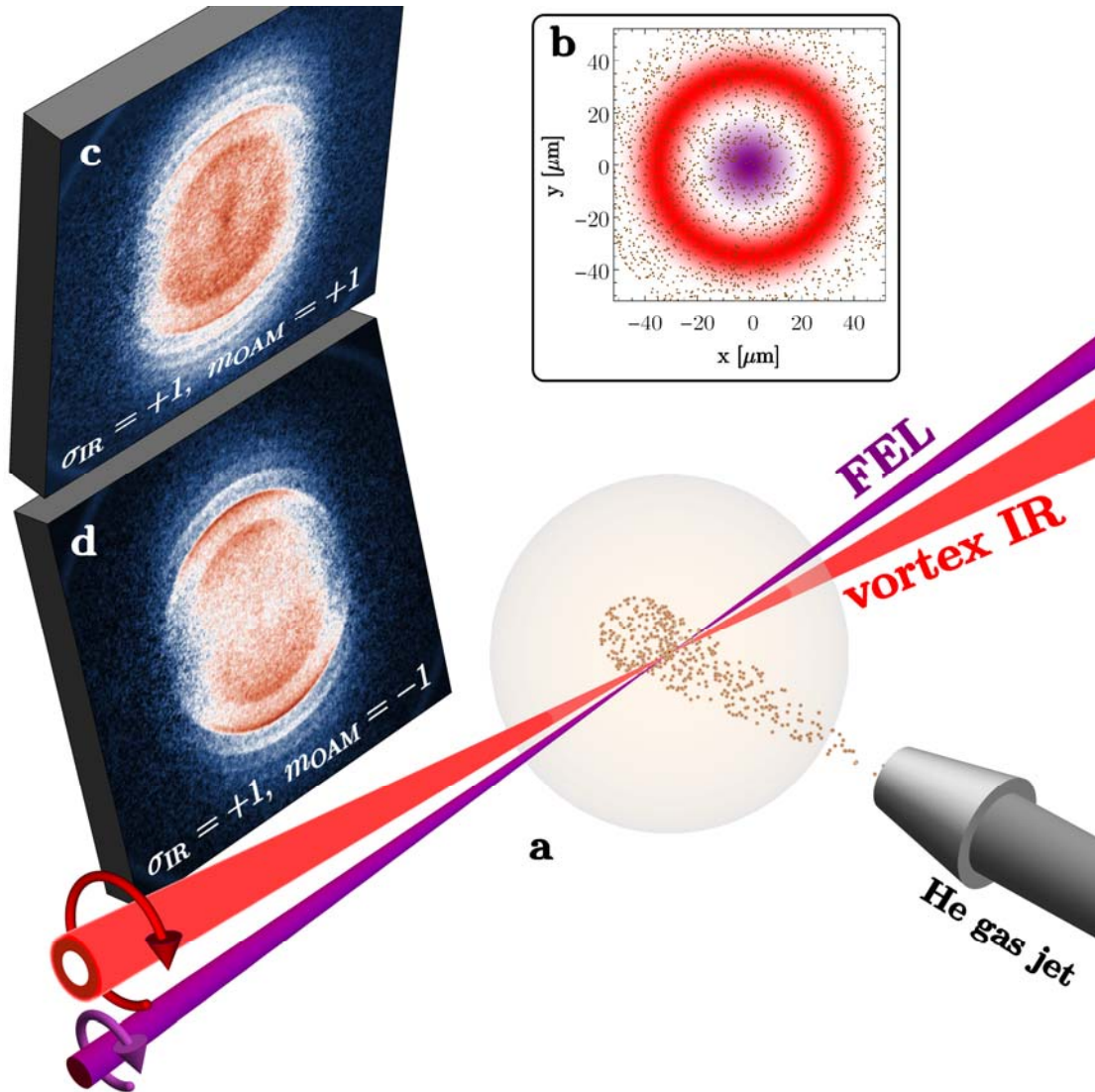343
344

345 **Figures**
346
347

Fig. 1 | Experimental setup and first evidence of OAM-dependent dichroism. **a**, Schematic representation of the experimental setup. The XUV light pulse is generated using a FEL. It has fixed (right-handed) circular polarization, a spot size of about 10 μm and intensity (at the sample position) of the order of 10^{18} W/m^2. The infrared laser beam has a spot size of about 60 μm and a power density in the range 0.5 - 4 x 10^{17} W/m^2. It provides variable circular (right and left-handed) polarization and can be made to carry a topological charge ($m_{\text{OAM}} = \pm 1$). Helium gas is injected into the experimental chamber (at room temperature) via a gas jet system. A VMI spectrometer is used to determine the angular distribution of the signal generated by the photoemitted electrons. **b**, Real-size XUV FEL (blue) and IR (red) spatial profiles at waist position. He atoms are also represented as dots with exaggerated dimensions. **c**, VMI image obtained for high IR intensity (about 3 x 10^{17} W/m^2), right-handed IR polarization and positive topological charge ($m_{\text{OAM}} = +1$). **d**, Same as panel c, with negative topological charge ($m_{\text{OAM}} = -1$).
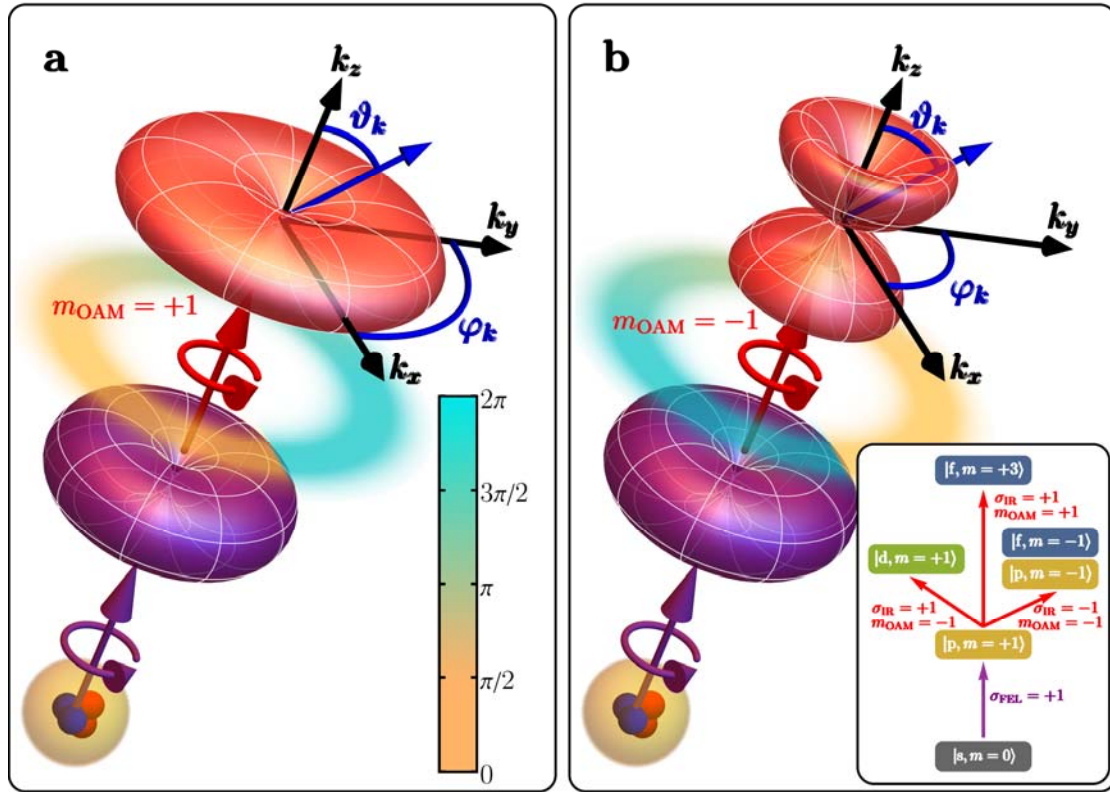
366
367
368

Figure 2

Fig. 2 | Theoretical description of the imprinting of light OAM on the matter wave of a single photoelectron released from a He atom. **a**, Ideal case of a single He atom placed at the centre of the OAM vortex. The photoelectron wave is launched by the VUV radiation (purple arrow), with right-handed circular polarization. This gives rise to a donut-like electron distribution extending in the plane perpendicular to light propagation. The photoemission process is assisted by an IR light vortex (red arrow), carrying right-handed circular polarization ($\sigma_{IR} = +1$) and a positive topological charge ($m_{OAM} = +1$, phase increasing clockwise). The vortex induces a quadrupole continuum-continuum transition, which leads to a donut-like electron distribution extending in the plane perpendicular to light propagation. For the simulations, an IR intensity of 0.7×10^{17} W/m^2 has been used. **b**, Same as panel a, with $m_{OAM} = -1$ (phase increasing counterclockwise). In this case, the vortex-spin combination induces a dipole transition, resulting in an electron distribution stretched in the direction of beam propagation. Inset: Selection rules for the different combinations of polarization and topological charge considered in the present work.
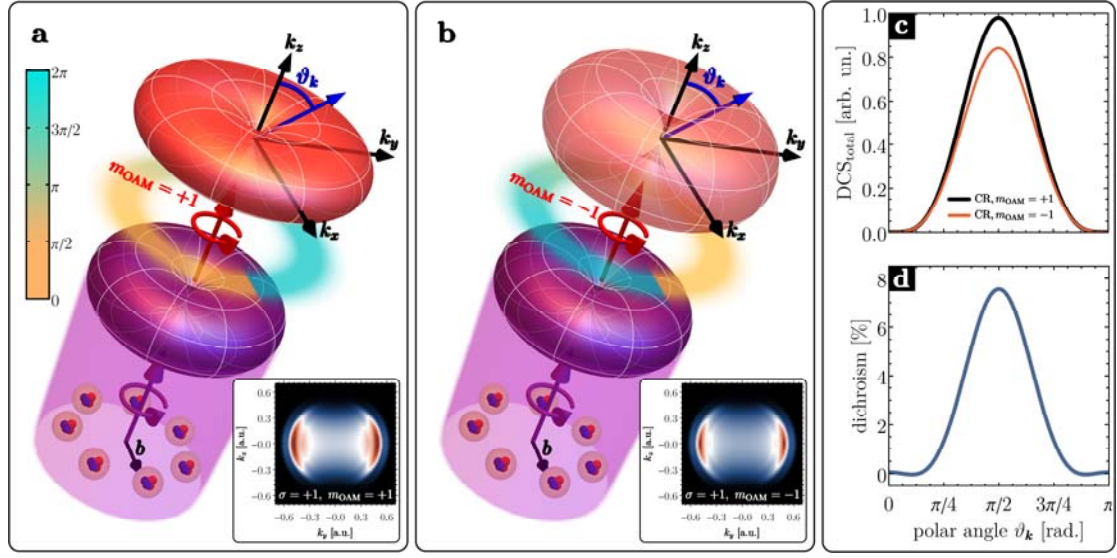
392

393 <u>**Figure 3**</u>

394

395

396

397 **Fig. 3 | Theoretical description of the imprinting of light OAM on the matter**
398 **waves of photoelectrons released from a sample of He atoms. a**, Sample of He
399 atoms placed at random positions ***b*** from the IR optical axis. The electron
400 distributions generated after sample's interaction with the FEL and IR beams have
401 been found by solving the theoretical problem for different values of ***b*** and averaging
402 the obtained results. The parameters are the same as in Fig. 2a; in particular, $\sigma_{\text{IR}} =$
403 $+1$ and $m_{\text{OAM}} = +1$. Inset: projection of the photoelectron distribution on the (k_y, k_z)
404 plane. **b**, Same as Fig. a, with $\sigma_{\text{IR}} = +1$ and $m_{\text{OAM}} = -1$. Inset: projection of the
405 photoelectron distribution on the (k_y, k_z) plane. **c**, DCSs obtained by integrating the
406 signal of the first sideband of the projected distributions shown in the insets of panels
407 (a) and (b), as a function of the polar angle. **d**, OAM-dependent dichroism, defined as
408 the difference between the curves shown in panel (c), normalized to their sum.

409

Figure 4
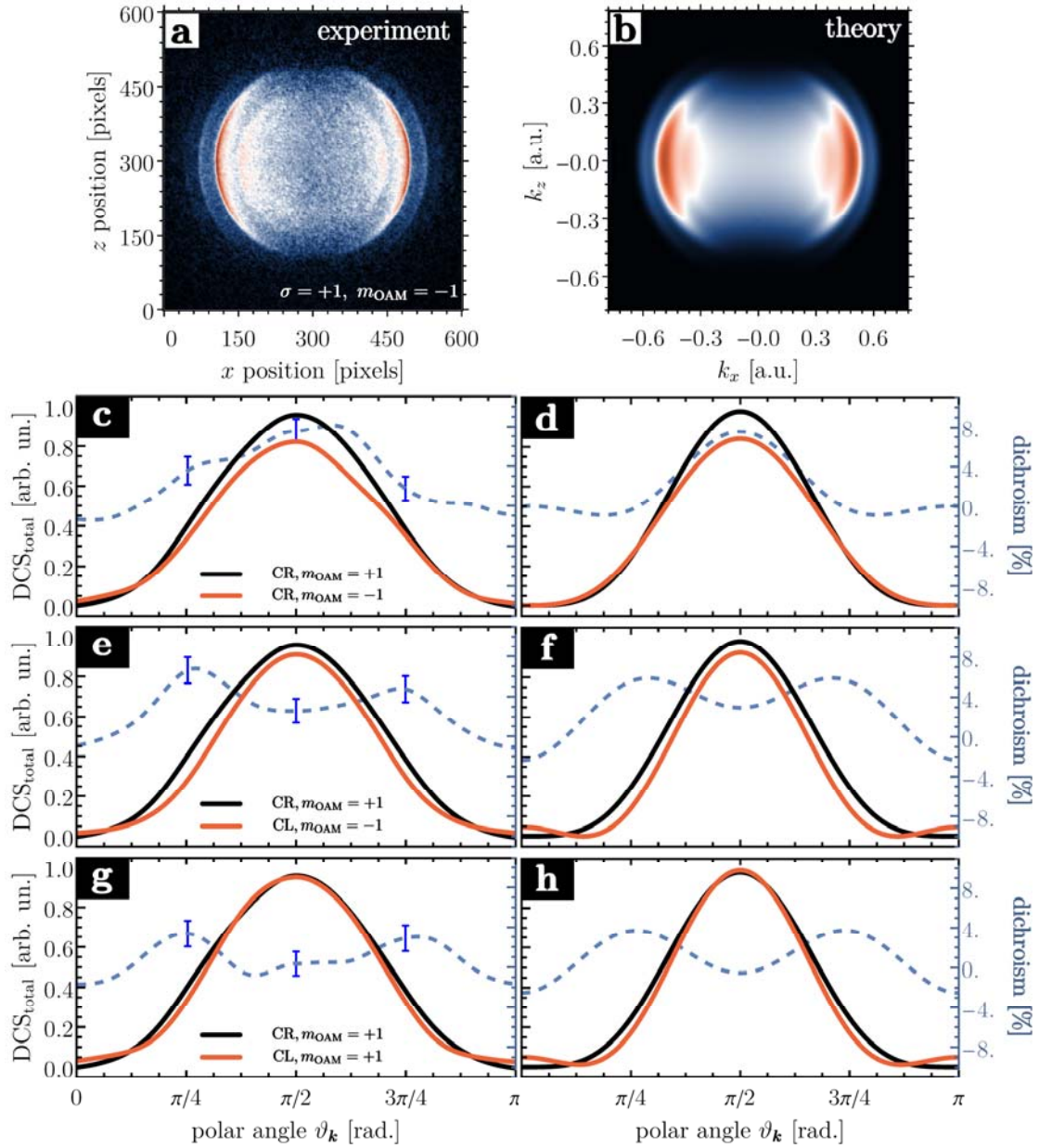
Fig. 4 | Experimental vs. theoretical photoelectron spectra and DCSs for different combinations of IR spin and OAM.
a, Experimental VMI spectrum for the combination $\sigma_{IR} = +1, m_{OAM} = -1$. **b**, Theoretical VMI spectrum for the same combination as in **a**. **c**, Continuous curves: experimental DCSs for the combinations $\sigma_{IR} = +1, m_{OAM} = +1$ and $\sigma_{IR} = +1, m_{OAM} = -1$. Dashed curve: corresponding dichroic contrast. **d**, Theoretical DCSs and dichroic contrast for the same combination as in **c**. **e**, Experimental DCSs and dichroic contrast for the combinations $\sigma_{IR} = +1, m_{OAM} = +1$ and $\sigma_{IR} = -1, m_{OAM} = -1$. **f**, Theoretical DCSs and dichroic contrast for the same combination as in **e**. **g**, Experimental DCSs and dichroic contrast for the combinations $\sigma_{IR} = +1, m_{OAM} = +1$ and $\sigma_{IR} = -1, m_{OAM} = +1$. **h**, Theoretical DCSs and dichroic contrast for the same combination as in **g**. For a discussion about the evaluation of error bars, see Methods.

427
428
429

References

[1] Allen, L. et al. Angular momentum of light and the transformation of Laguerre-Gaussian laser modes. *Phys. Rev. A* **45**, 8185 (1992).

[2] Kaneyasu, T. et al. Limitations in photoionization of helium by an extreme ultraviolet optical vortex. *Phys. Rev. A* **95,** 023413 (2017).

[3] Schmiegelow, C. T. et al. Transfer of optical orbital angular momentum to a bound electron. Nat. Commun. 7, 12998 (2016).

[4] Afanasev, A. et al. Experimental verification of position-dependent angular-momentumselection rules for absorption of twisted light by a bound electron. *New J. Phys.* **20** 023032 (2018).

[5] Allaria, E. et al. Highly Coherent and Stable Pulses from the FERMI Seeded Free-Electron Laser in the Extreme Ultraviolet. *Nat. Photonics* **6**, 699 (2012).

[6] Köksal, K, Berakdar, J. Charge-current generation in atomic systems induced by optical vortices. *Phys. Rev. A* **86**, 063812 (2012).

[7] Picón, A., Mompart, J., Vázquez de Aldana, J.R., Plaja, L., Calvo, G.F., Roso, L. Photoionization with orbital angular momentum beams. *Opt. Express* **18**, 3660 (2010).

[8] Wätzel J., Pavlyukh Y., A Schäffer A.F., Berakdar J. Optical vortex driven charge current loop and optomagnetism in fullerenes *Carbon* 99, 439 (2016).

[9] Lyamayev, V. A modular end-station for atomic, molecular, and cluster science at the low density matter beamline of FERMI@Elettra. *J. Phys. B* **46**, 164007 (2013).

[10] Glover, T. E., Schoenlein, R. W., Chin, A. H. & Shank, C. V. Observation of laser assisted photoelectric effect and femtosecond high order harmonic radiation. Phys. Rev. Lett. **76,** 2468 (1996).

[11] Meyer, M., Costello, J. T., Düsterer, S., Li, W. B. & Radcliffe, P. Two-colour experiments in the gas phase. *J. Phys. B* **43**, 194006 (2010).

[12] O'Keeffe, P. et al., Polarization effects in two-photon nonresonant ionization of argon with extreme-ultraviolet and infrared femtosecond pulses. *Phys. Rev. A* **69,** 051401 (2004).

[13] Meyer, M. et al. Polarization Control in Two-Color Above-Threshold Ionization of Atomic Helium. *Phys. Rev. Lett.* **101**, 193002 (2008).

[14] Guyétand, O. et al. Evolution of angular distributions in two-colour, few-photon ionization of helium, *J. Phys. B: At. Mol. Opt. Phys.* **41**, 051002 (2008).

[15] Haber, L.H., Doughty, B., Leone, S.R. Photoelectron Angular Distributions and Cross Section Ratios of Two-Color Two-Photon Above Threshold Ionization of Argon. *J. Phys. Chem. A* **113**, 4713152 (2009).

[16] Haber, L.H., Doughty, B., Leone, S.R. Energy-dependent photoelectron angular distributions of two-color two-photon above threshold ionization of atomic helium. *Phys. Rev. A* **84**, 013416 (2011).

[17] O'Keeffe, P. et al. Near-threshold photoelectron angular distributions from two-photon resonant photoionization of He. *New J. Phys* **15**, 013023 (2013).

[18] Grum-Grzhimailo, A.N., Gryzlova, E.V. Nondipole effects in the angular distribution of photoelectrons in two-photon two-color above-threshold atomic ionization. *Phys. Rev. A* **89** 043424-1 (2014).

[19] Taïeb R. et al. Circular dichroism from unpolarized atoms in multiphoton multicolor ionization. *Phys. Rev. A* **62**, 013402 (2000).

[20] Kazansky, A.K., Grigorieva, A.V., Kabachnik, N.M. Circular Dichroism in Laser-Assisted Short-Pulse Photoionization. *Phys. Rev. Lett.* **107**, 253002 (2011).

479 [21] Mazza, T. et al., Determining the polarization state of an extreme ultraviolet free-
480 electron laser beam using atomic circular dichroism. *Nat. Commun.* **5,** 3648 (2014).
481 [22] Quinteiro, G.F., Schmidt-Kaler, F., Schmiegelow, C.T., Twisted-Light–Ion
482 Interaction: The Role of Longitudinal Fields. Phys. Rev. Lett. **119**, 253203 (2017).
483 [23] Vrakking, M. J. J. An iterative procedure for the inversion of two-dimensional
484 ion/photoelectron imaging experiments. *Rev. Sci. Instrum.* **72**, 4084 (2001).
485 [24] Zangrando, M. et al. PADReS: the photon analysis delivery and reduction system
486 at the FERMI@Elettra FEL user facility. *Rev. Sci. Instrum.* **80**, 305 (2009).
487 [25] Raimondi, L. et al. Kirkpatrick–Baez active optics system at FERMI: system
488 performance analysis. *J. Synchrotron Rad.* **26**, 1462 (2019).
489 [26] Svetina, C et al. The Low Density Matter (LDM) beamline at FERMI: optical
490 layout and first commissioning, J. Synchrotron Rad. **22**, 538 (2015).
491 [27] Sarsa, A., Gálvez, F., Buendia, E. Parameterized optimized effective potential for
492 the ground state of the atoms He through Xe. *At. Data Nucl. Data Tables* **88**, 163
493 (2004).
494
495
496
497
498
499
500
501
502
503
504